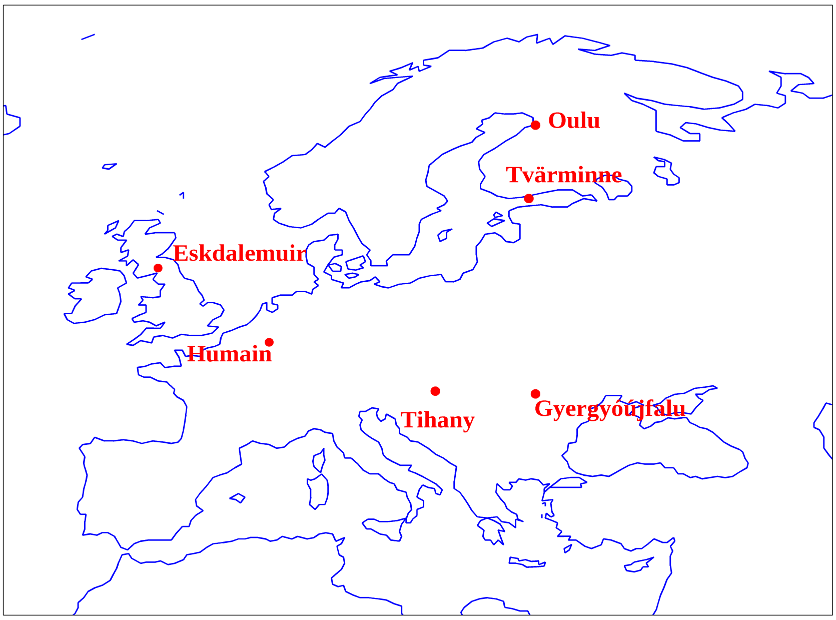

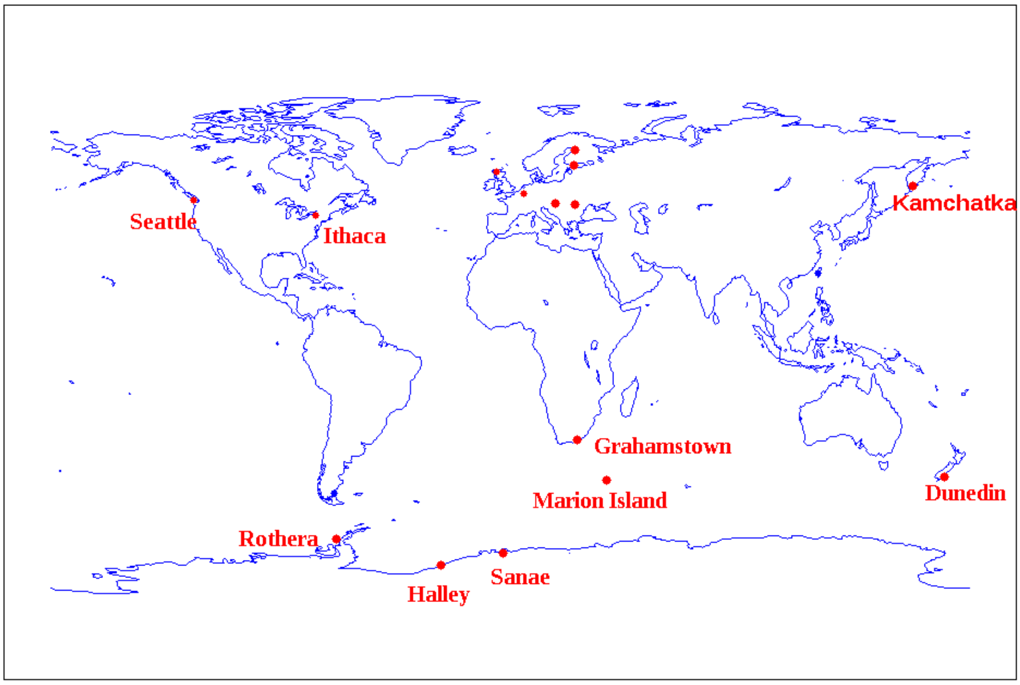

Figure 1.1. AWDANet nodes with AWA installed in PLASMON. Top panel: European nodes. Bottom panel: nodes in the rest of the world.

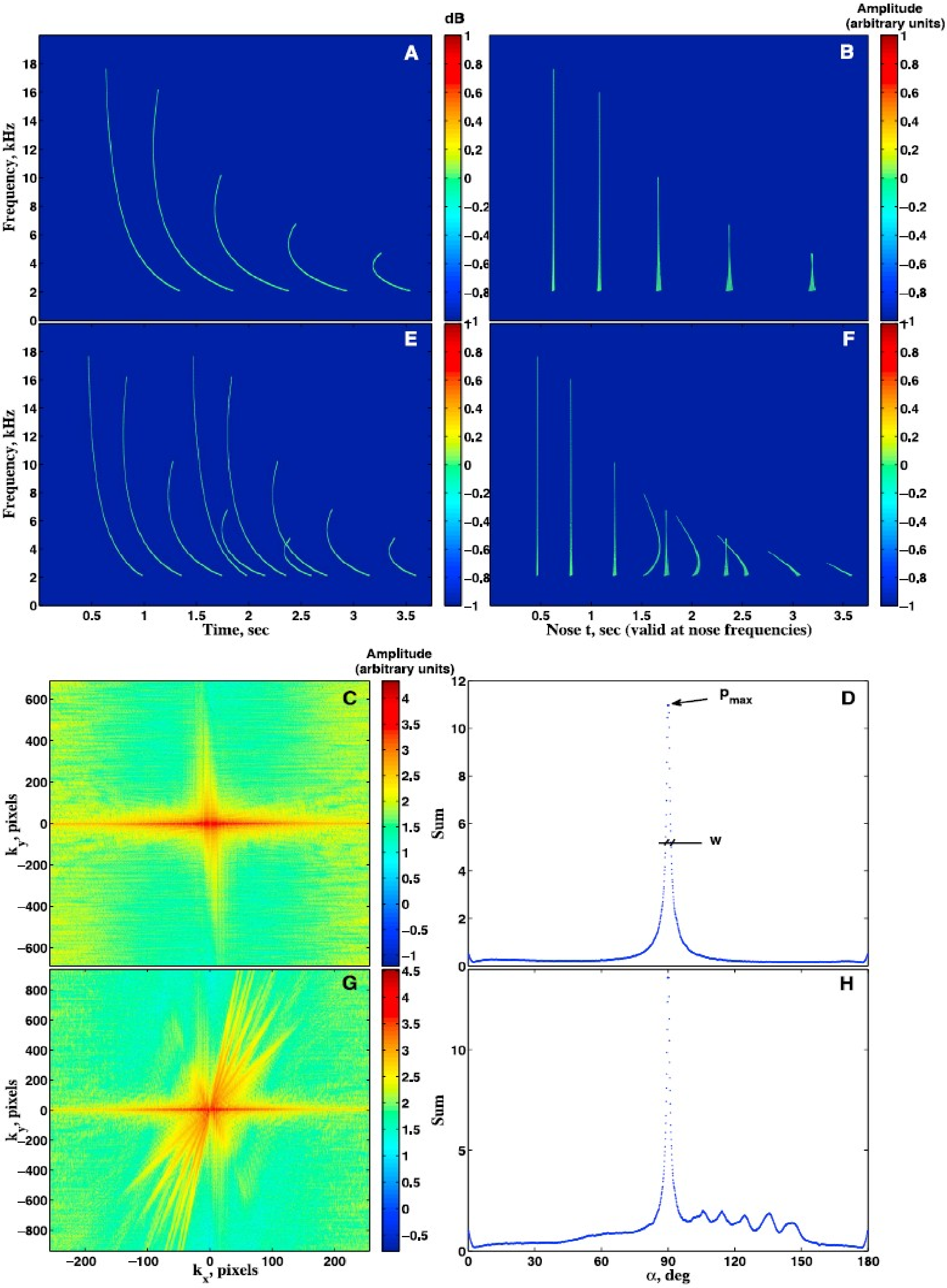

Figure 1.2. VTT and 2D FFT applied to a model MP whistler group (a, b, c, and d) and to an overlapping model MP whistler group (e, f, g, and h). (a and e) Spectrogram of the whistler group, (b and f) VTT of the whistler group in a and e, (c and g) 2D FFT image (absolute value) of VTT matrix, and (d and h) sum of the 2D FFT image along the lines drawn through the center of the image, in arbitrary units. The sums were calculated up to 256 points from the center of the image in all directions. Note that α is measured from vertical.

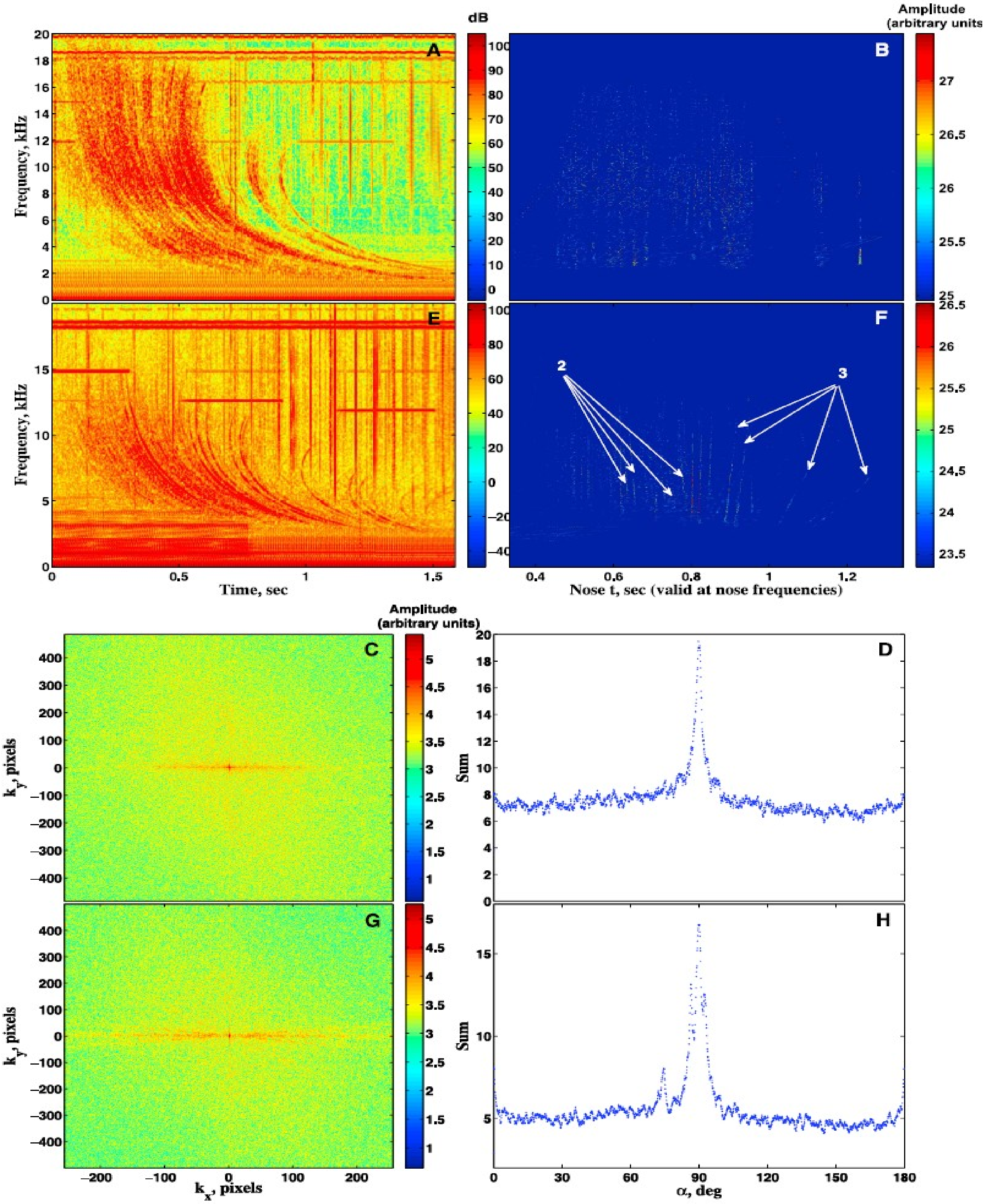

Figure 1.3. Same as Figure 1.2 but applied to naturally occurring whistlers. (a, b, c, and d) A MP whistler group recorded in Dunedin, New Zealand at 1150:23 UT on 4 February 2006 and (e, f, g, and h) a whistler recording exhibiting overlapping MP groups, recorded in Dunedin, New Zealand at 0430:50 UT on 23 July 2007. b and f showing VTT matrix that are very difficult to visualize, because VTT matrix is almost empty (there are 10,000 nonzero elements in the 1024 × 1600 matrix).The best view can be achieved by zooming it up to at least 150% on a computer screen.

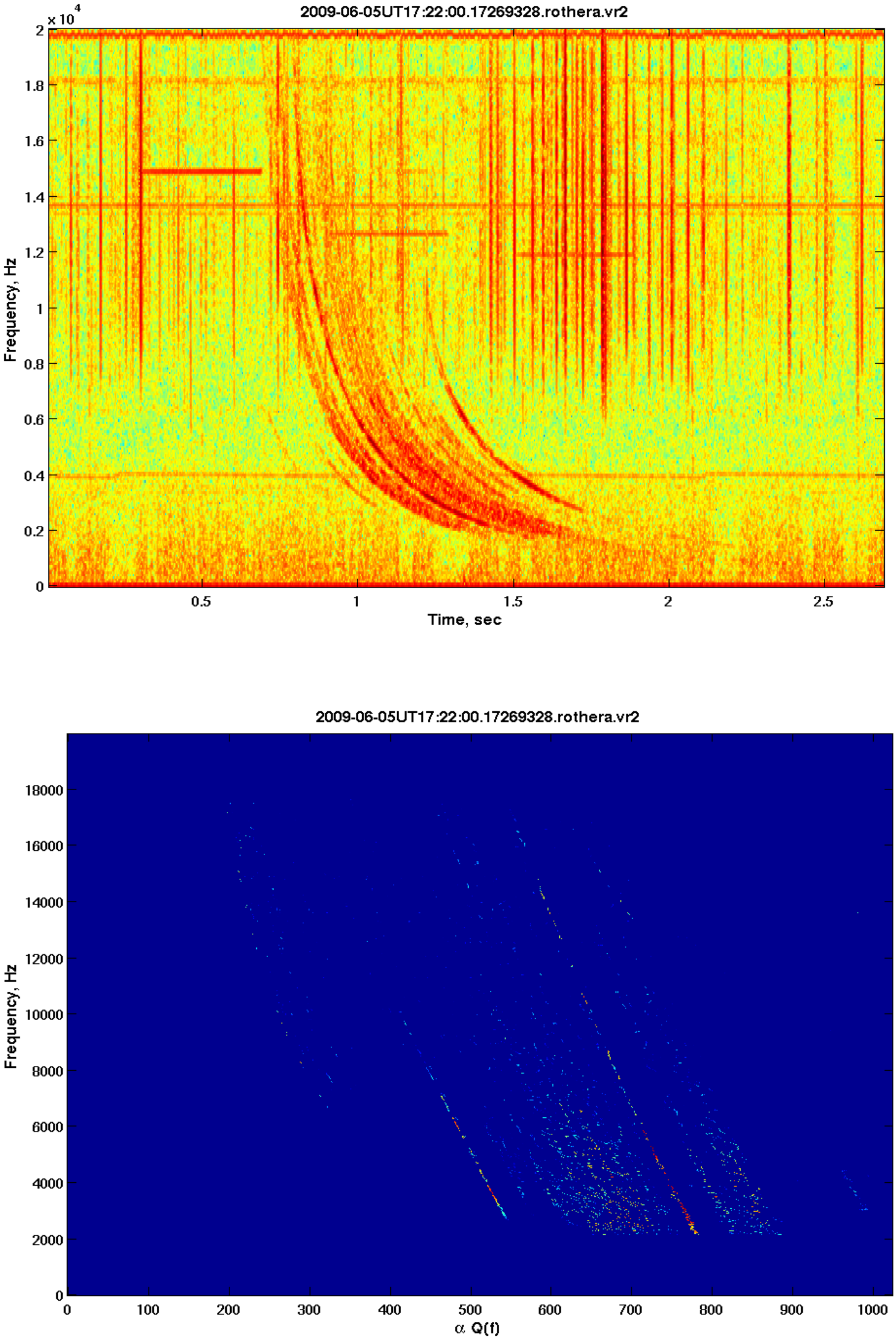

Figure 1.4. Top panel : spectrogram matrix; bottom panel: Q-transformation

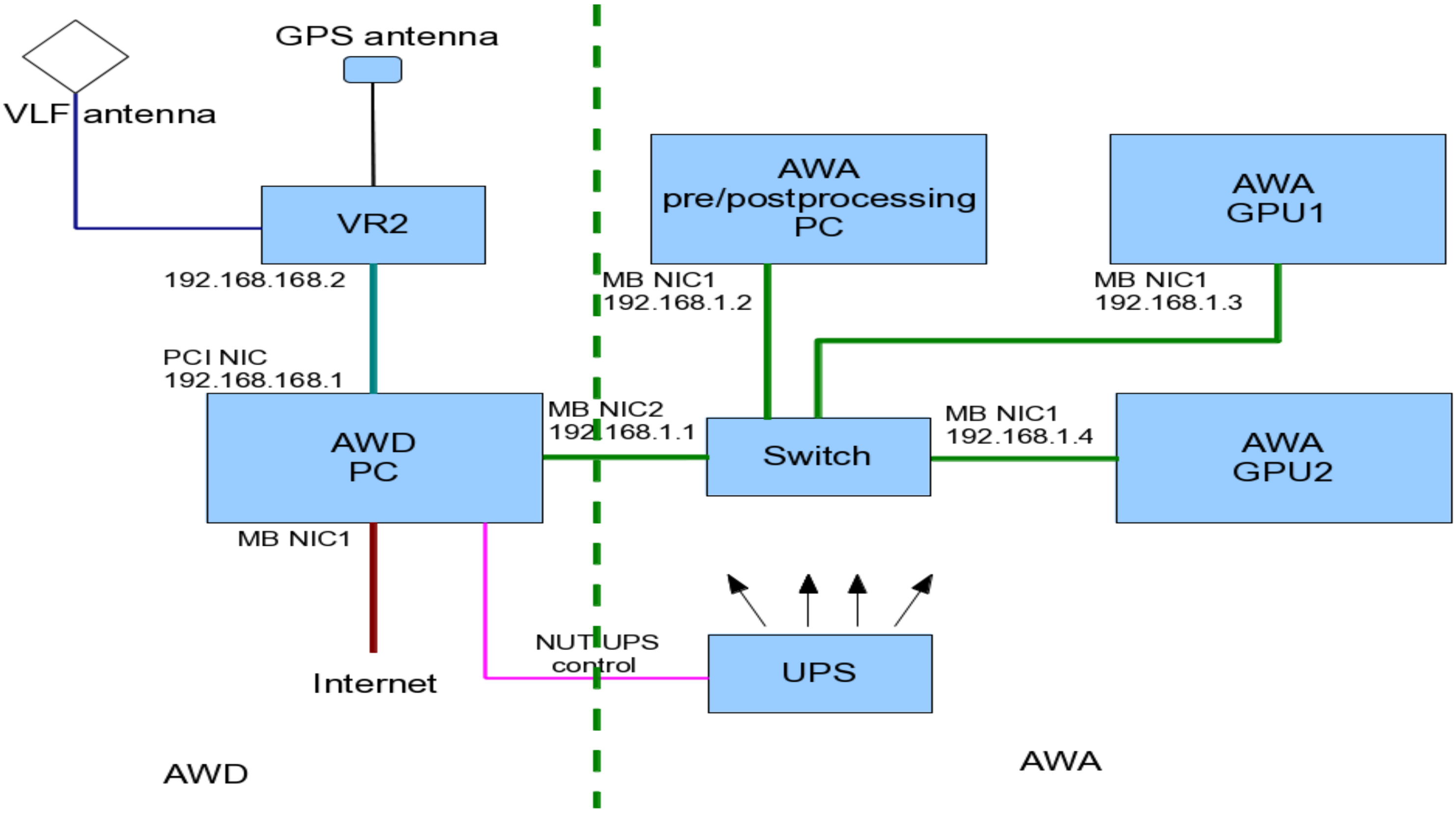

Figure 1.5. Configuration of AWDANet nodes with AWA

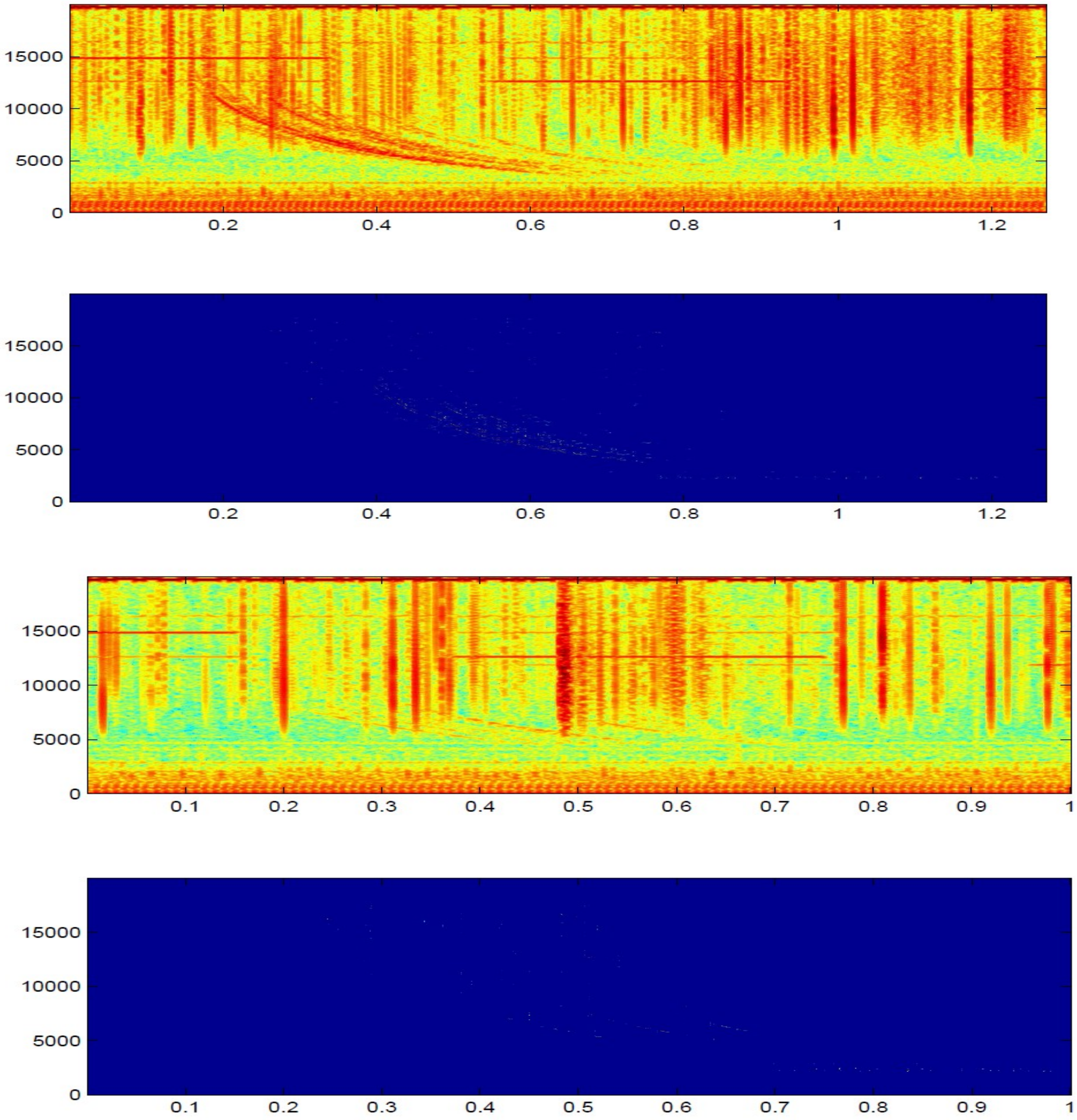

Figure 1.6. QF=00 (top panel and QF-06 (bottom panel) . This image can be viewed at zoom=400% to see the the details of simplified reassigned spectrograms.

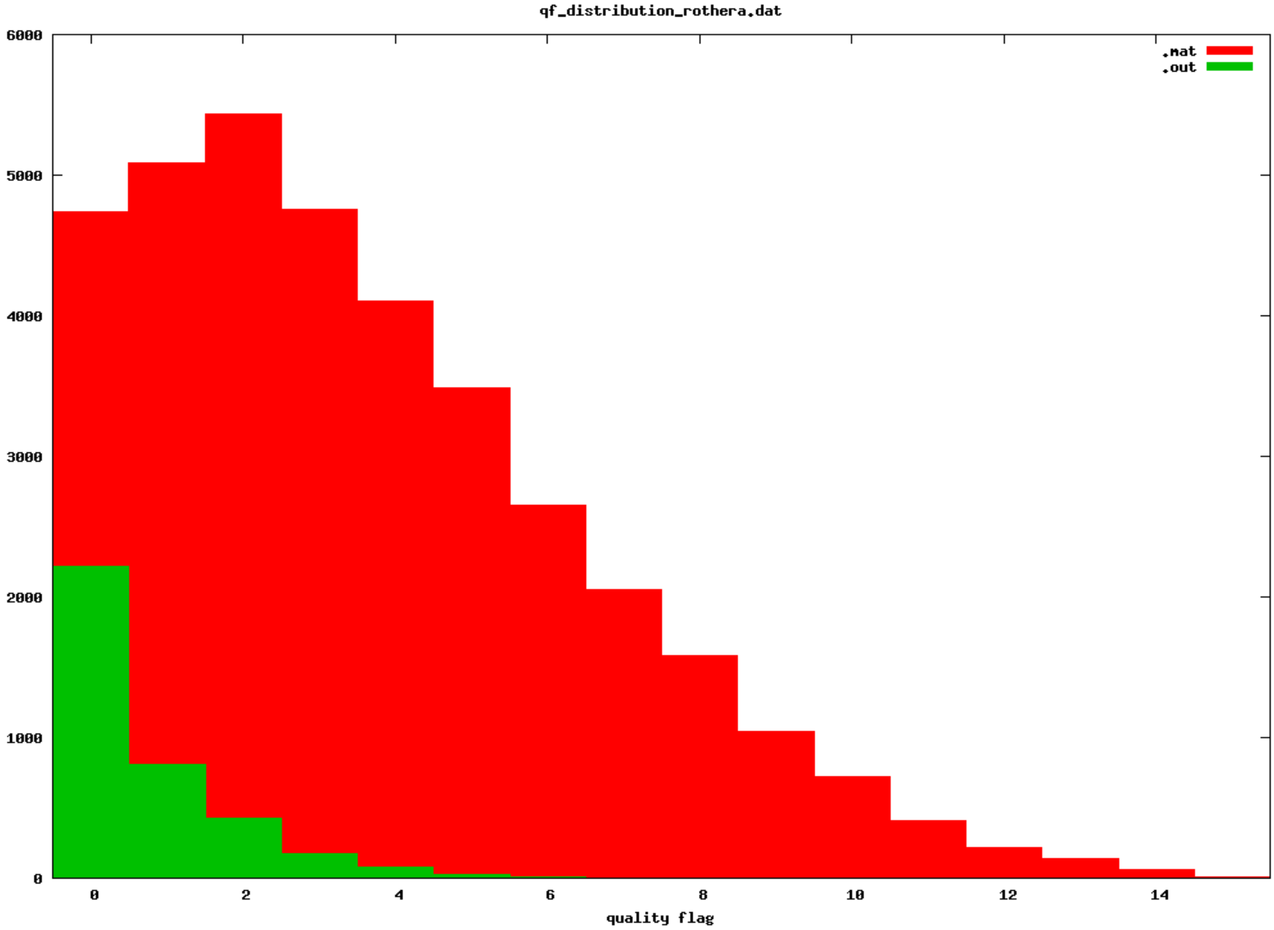

Figure 1.7. QF statistics collected at Rothera. The red bars are the pre-processed events, the greens are the successfully inverted ones.

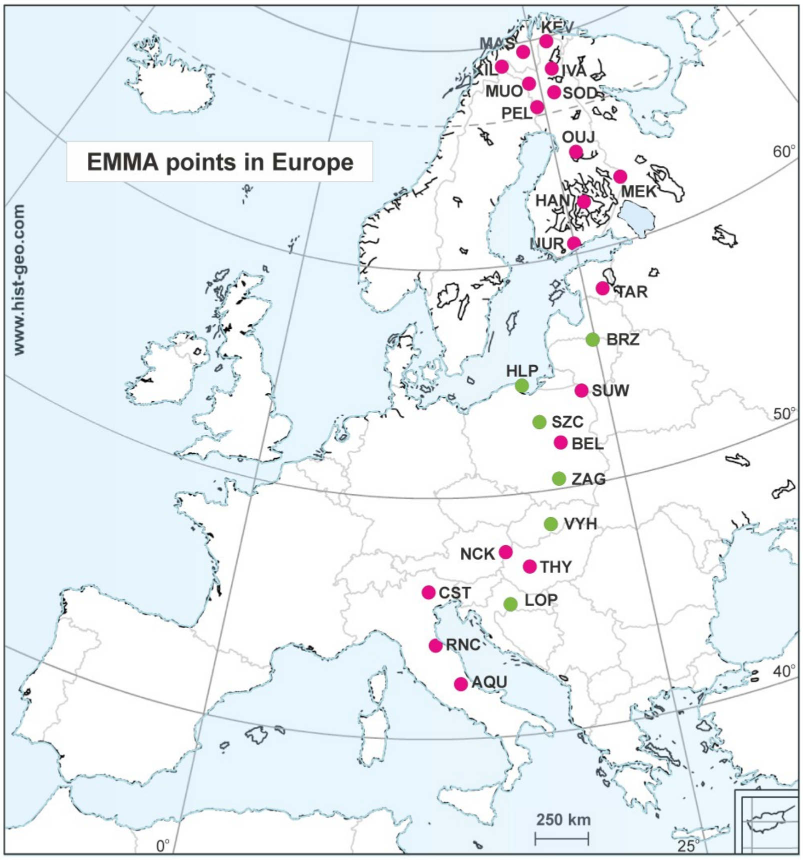

Figure 2.1. EMMA stations across Europe. The new stations installed in PLASMON are LOP, VYH, ZAG, SZC, HLP, and BRZ (green dots).

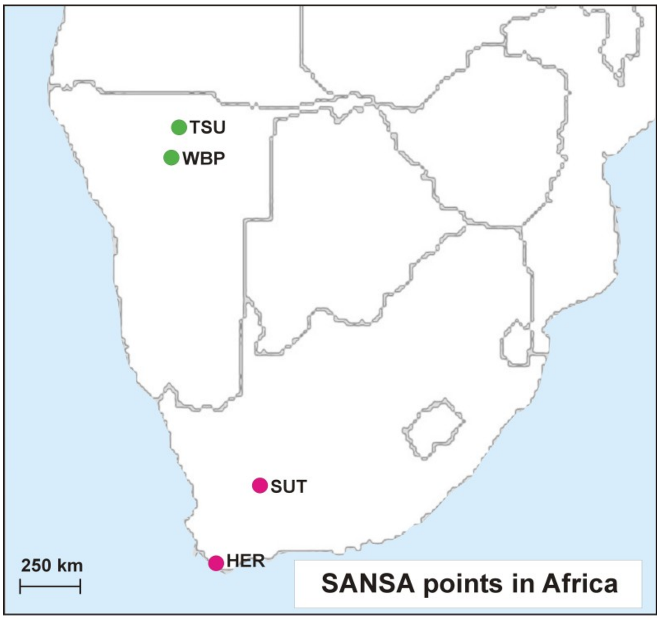

Figure 2.2. SANSA stations in South Africa. The new stations installed in PLASMON are WBP and TSU (green dots).

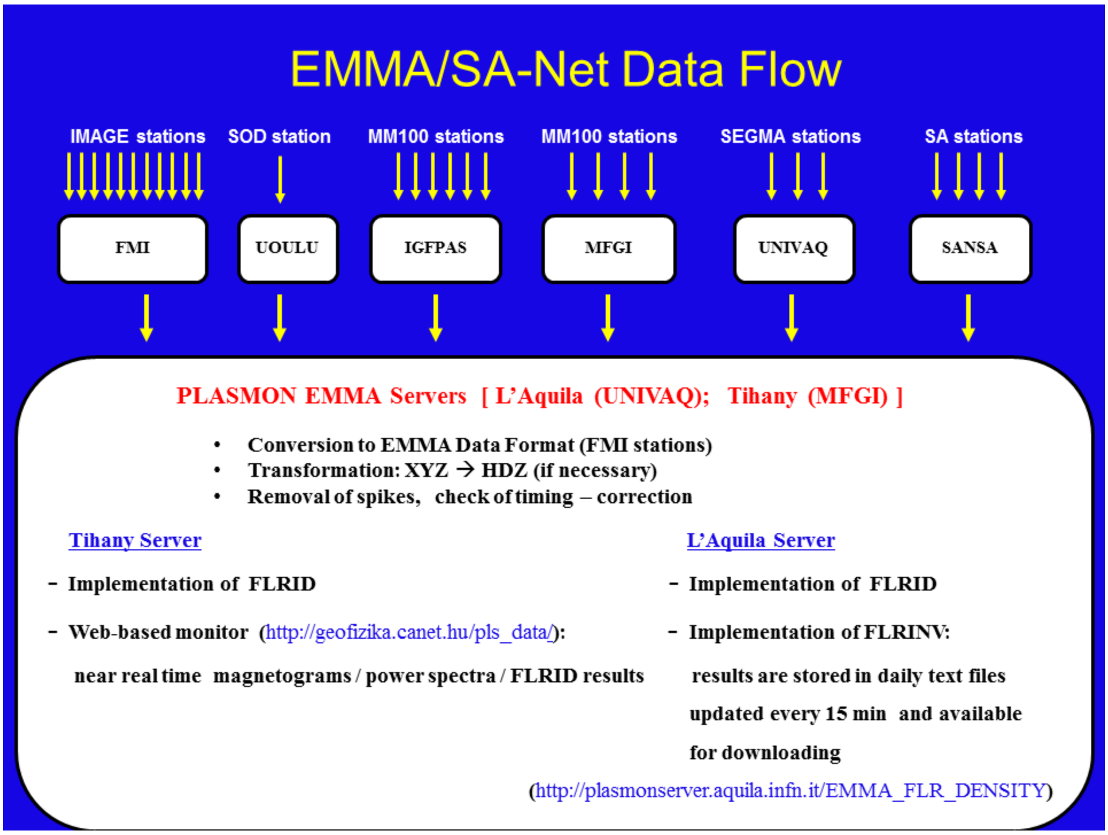

EMMA/SA-Net Data Flow

IMAGE stations SOD station MM100 stations MM100 stations SEGMA stations SA stations

FMI UOULU IGFPAS MFGI UNIVAQ SANSA

PLASMON EMMA Servers [L'Aquila (UNIVAQ); Tihany (MFGI)]

- Conversion to EMMA Data Format (FMI stations)
- Transformation: XYZ → HDZ (if necessary)
- Removal of spikes, check of timing – correction

Tihany Server

- Implementation of FLRID
- Web-based monitor (http://geofizika.canet.hu/pls_data/):

near real time magnetograms / power spectra / FLRID results

L'Aquila Server

- Implementation of FLRID
- Implementation of FLRINV:

results are stored in daily text files updated every 15 min and available for downloading (http://plasmonserver.aquila.infn.it/EMMA_FLR_DENSITY)

Figure 2.3. Scheme of the cyclical (every 15 min) sequence of operations starting from the data collection at the EMMA/SANSA networks up to the evaluation of the equatorial plasma mass density at different L-shells in near real time.

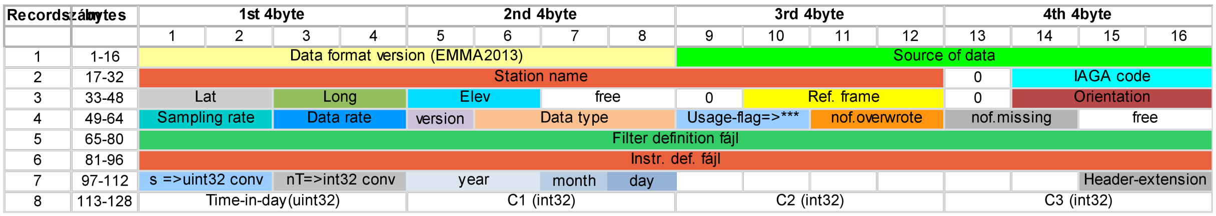

Recordszám	bytes	1st 4byte				2nd 4byte				3rd 4byte				4th 4byte			
		1	2	3	4	5	6	7	8	9	10	11	12	13	14	15	16
1	1-16	Data format version (EMMA2013)								Source of data							
2	17-32	Station name												0	IAGA code		
3	33-48	Lat		Long		Elev		free		0	Ref. frame			0	Orientation		
4	49-64	Sampling rate		Data rate		version	Data type			Usage-flag=>***		nof.overwrote		nof.missing		free	
5	65-80	Filter definition fájl															
6	81-96	Instr. def. fájl															
7	97-112	s =>uint32 conv		nT=>int32 conv		year		month	day							Header-extension	
8	113-128	Time-in-day(uint32)				C1 (int32)				C2 (int32)				C3 (int32)			

Figure 2.4. Structure and content of the header of the EMMA Data Format.

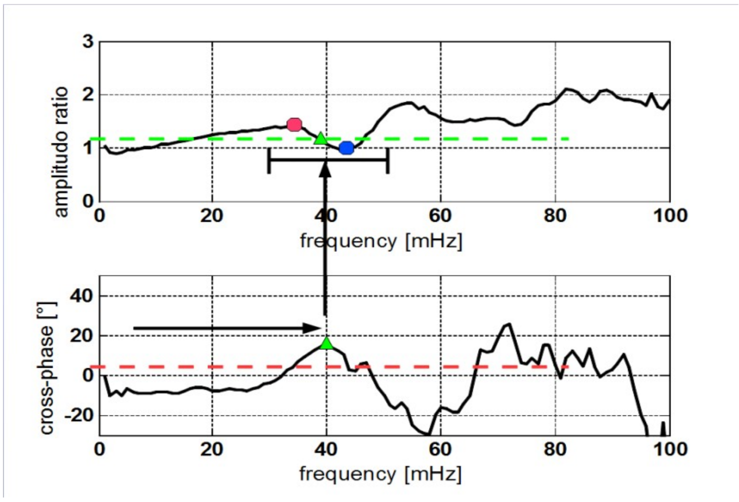

Figure 2.5. Amplitude ratio and cross phase spectra for a specific time. The figure illustrates the main steps of FLRID.

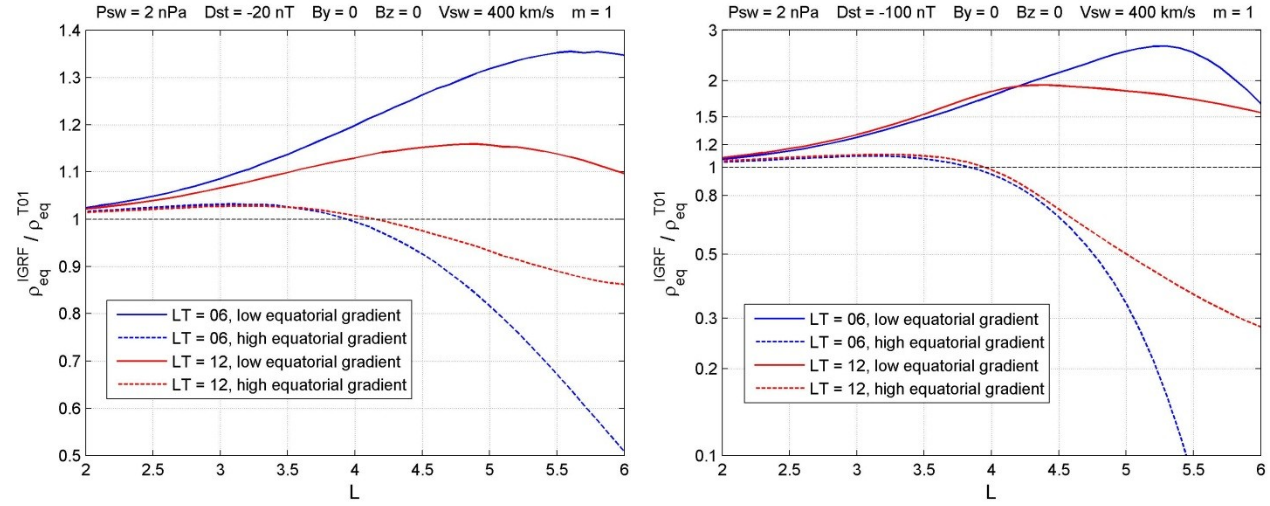

Figure 2.6. Ratio of equatorial plasma mass densities obtained using the IGRF model to those obtained using the T01 model versus *L*-shell for different conditions. Left panel refers to average solar wind/magnetospheric conditions and the right panel to disturbed magnetospheric conditions (Dst = −100). ρ_{eq}^{T01} values are scaled to the equatorial crossing point of the IGRF line using the empirical low $\rho_{eq} = \rho_{eq,o} \times 10^{-B(L-Lo)}$, where *Lo* is the radial distance of the equatorial crossing point of the T01 line and *B* is a parameter assumed to range between 0.3 and 0.9.

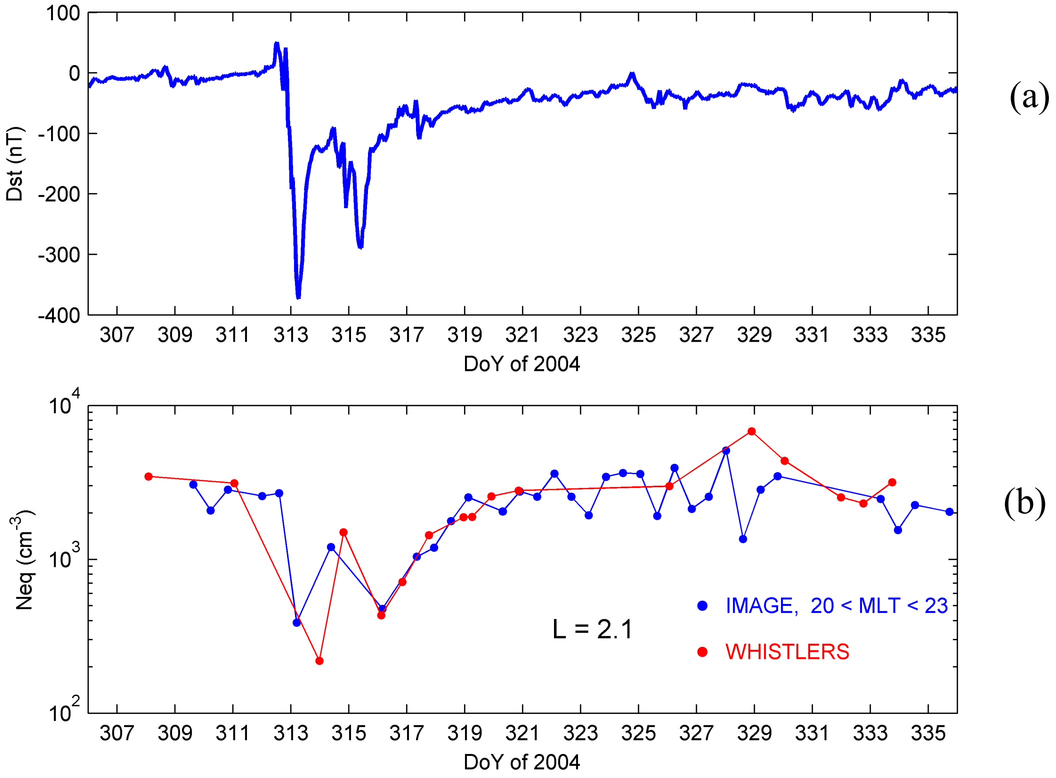

Figure 2.7. a) Dst values for November 2004; b) IMAGE-RPI electron density measurements (blue) and equatorial electron densities obtained from Tihany whistlers (red).

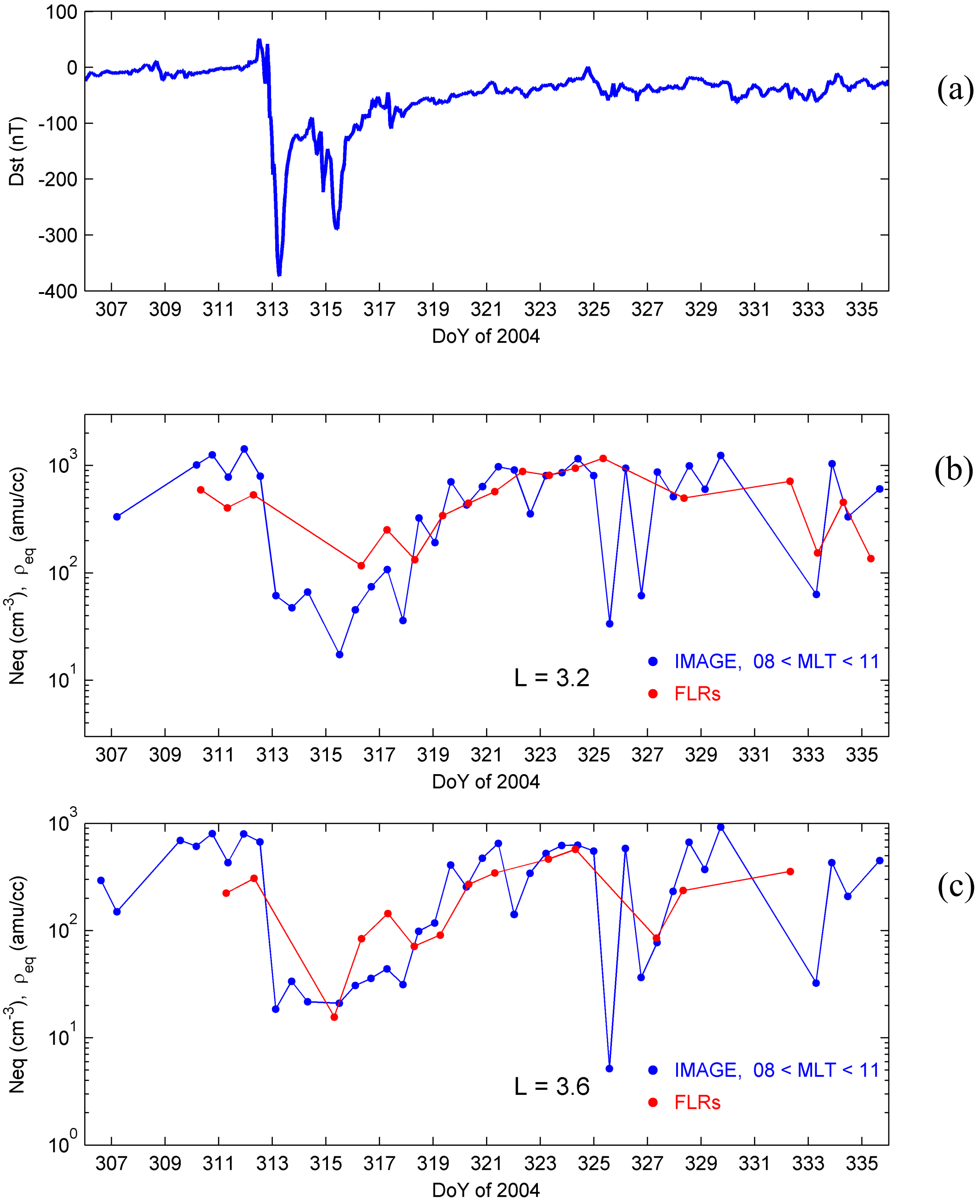

Figure 2.8. a) Dst values for November 2004; b) IMAGE-RPI electron density measurements (blue dots) and equatorial plasma mass densities obtained from FLRs for $L = 3.2$ (red dots); c) the same as (b) but for $L = 3.6$ FLRs.

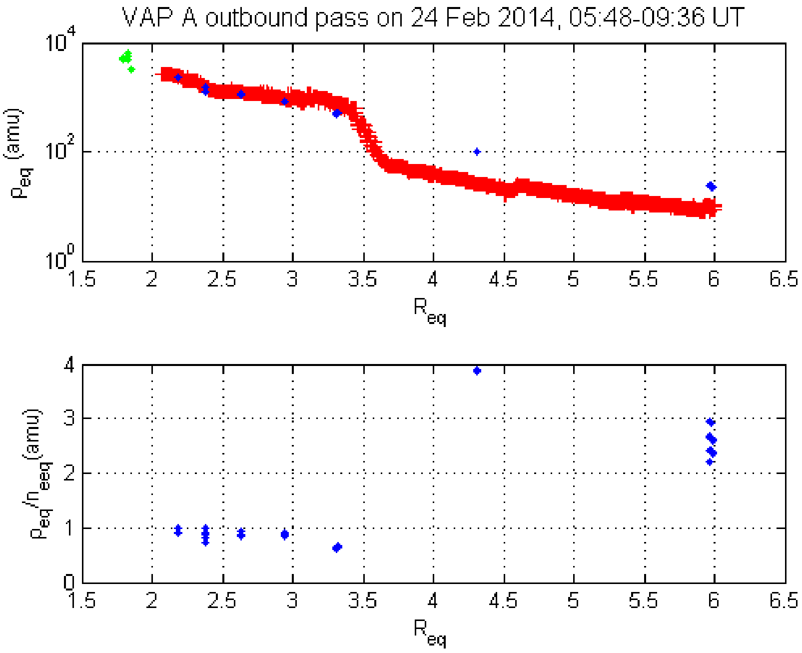

Figure 2.9. Radial profiles of electron densities from VAP A-EMFISIS (red crosses) and mass densities derived from FLRs at EMMA (green and blue dots) on 24 Feb, 2014 05:48-09:36 (outbound pass).

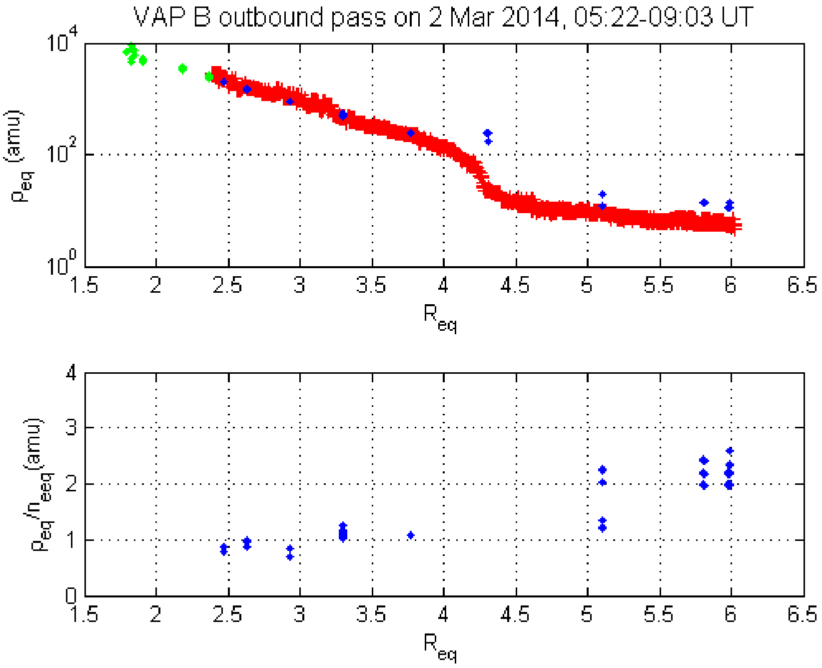

Figure 2.10. Radial profiles of electron densities from VAP B-EMFISIS (red crosses) and mass densities derived from FLRs at EMMA (green and blue dots) on 2 March, 2014 05:22-09:03 (inbound pass).

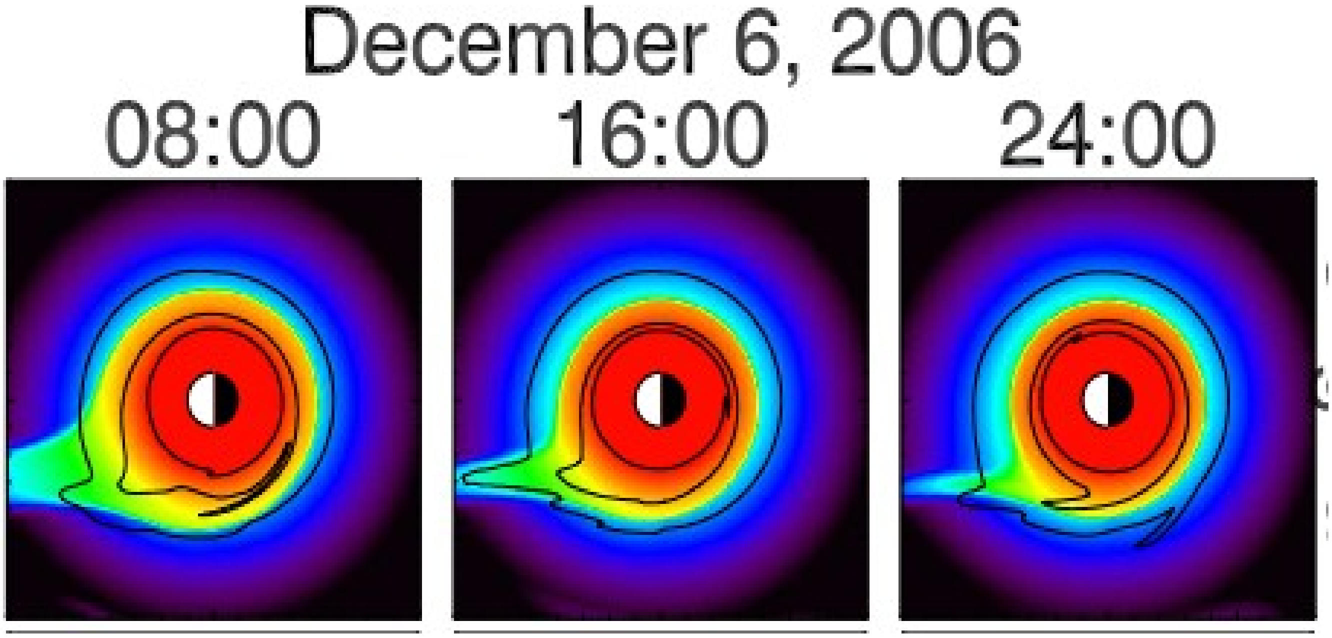

Figure 3.1 Snapshots of the DGCPM running

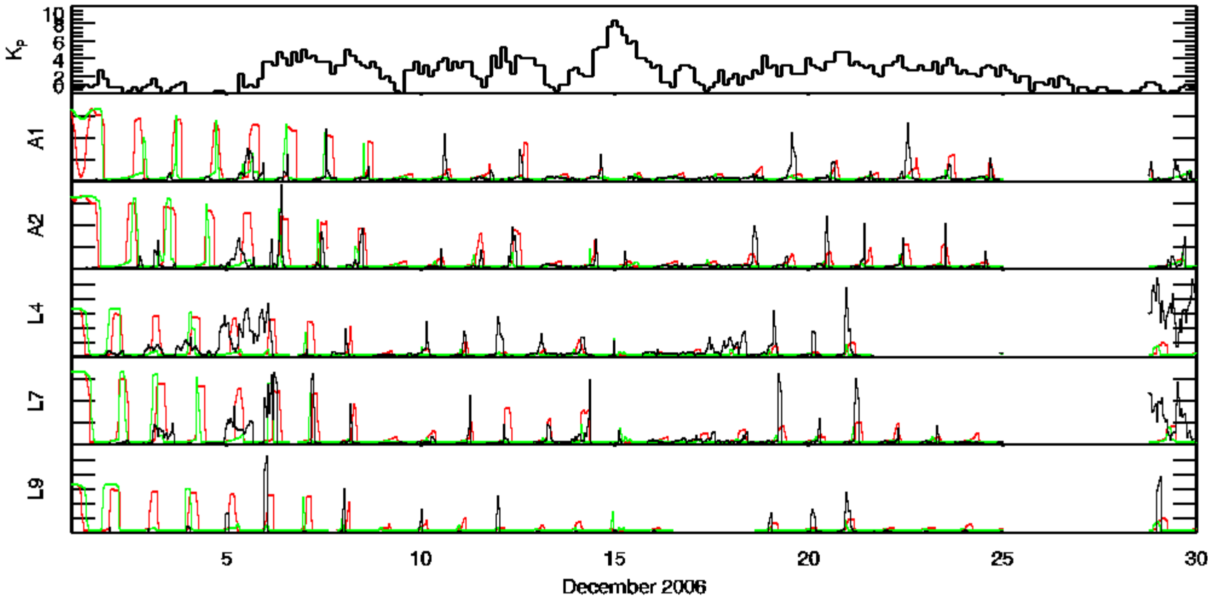

Figure 3.2. Comparison between the DGCPM and density observation from LANL satellites.

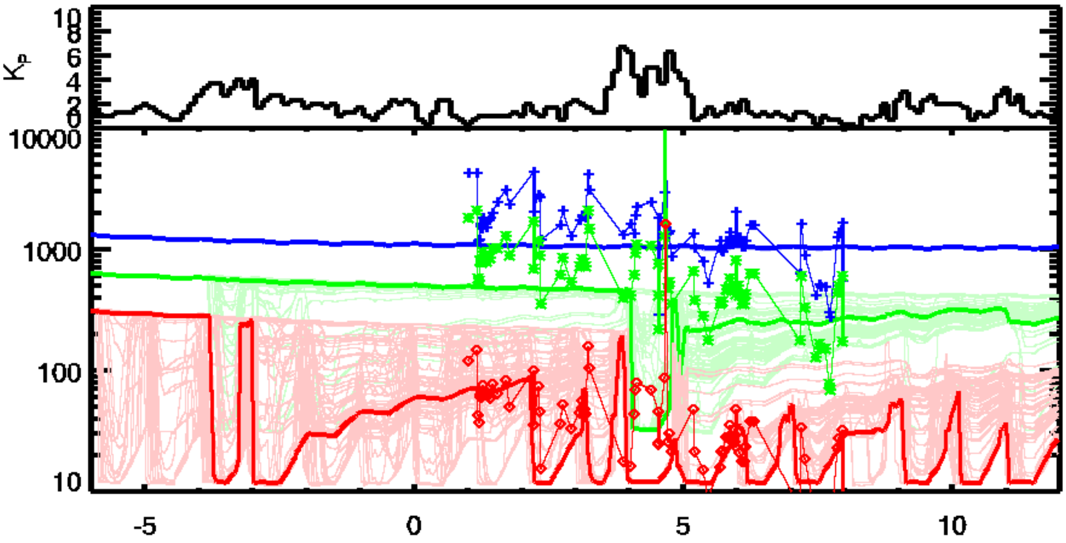

Figure 3.3. Initial comparison between the DGCPM and the VLF inversion algorithm output.

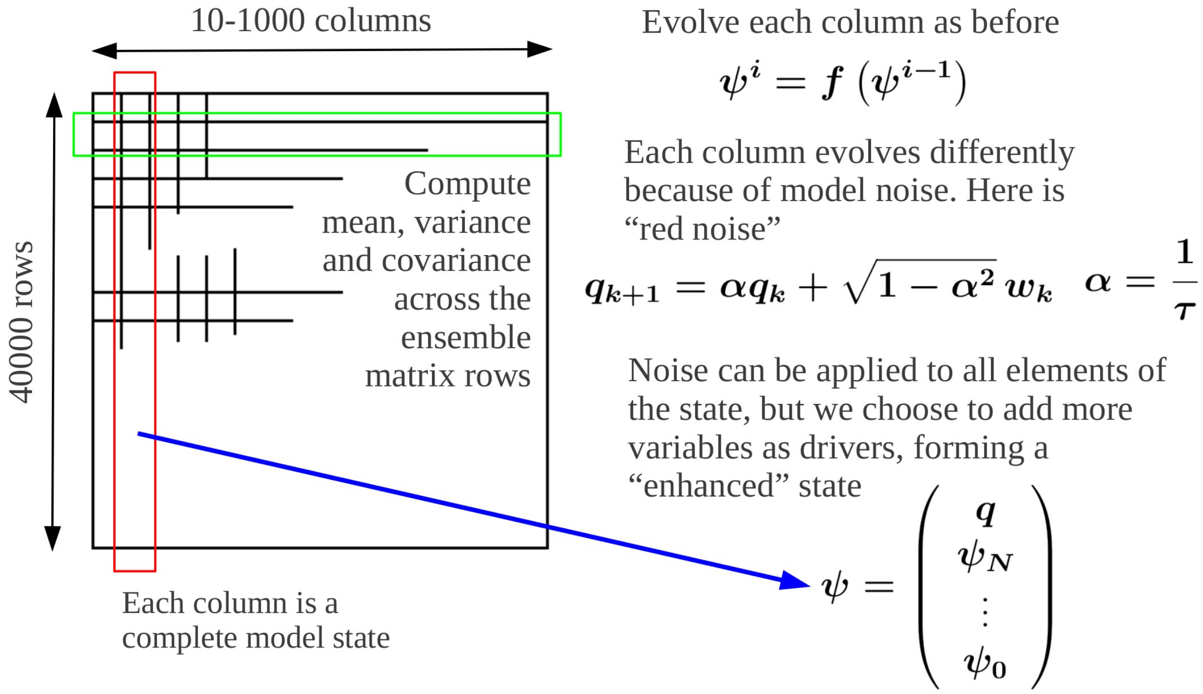

Figure 3.4. Illustration of the matrix representation of the models in the EnKF, and of the red noise model used.

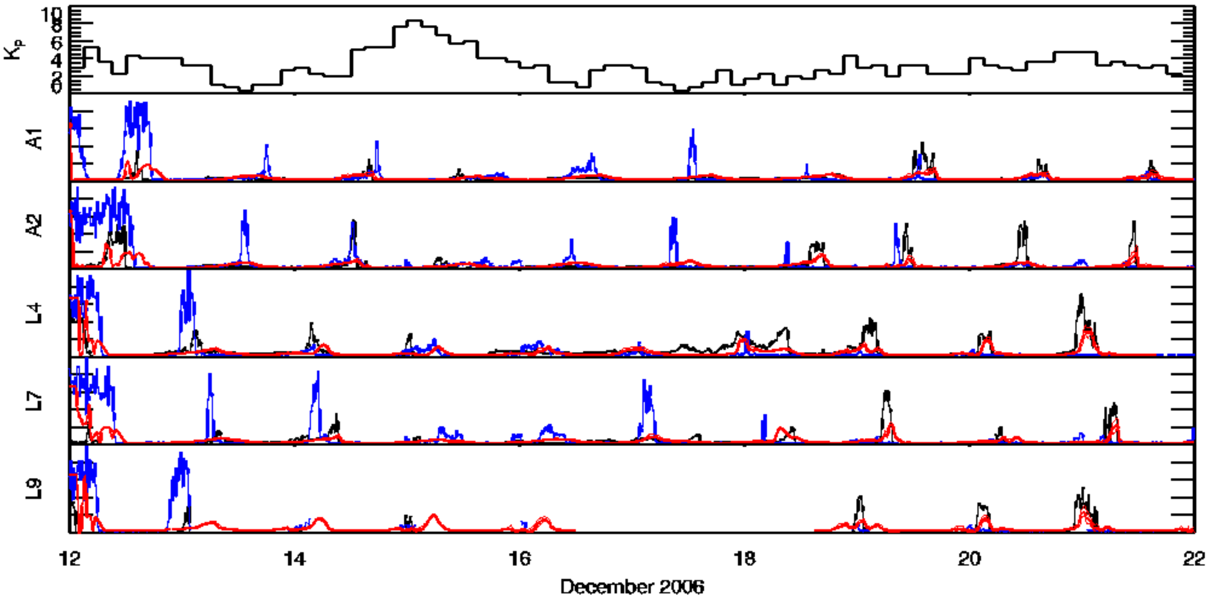

Figure 3.5. Assimilation with density measurements from the LANL geostationary satellites. The black traces are the LANL observations. The blue traces are the DGCPM model run without data assimilation.

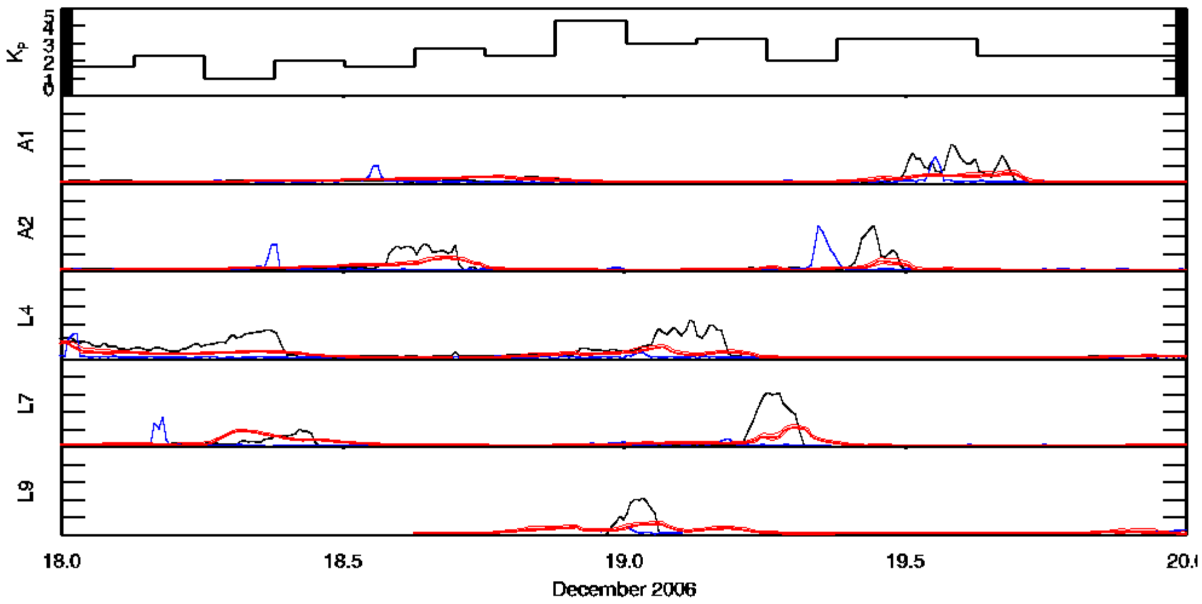

Figure 3.6. Assimilation with density measurements from the LANL geostationary satellites. The black traces are the LANL observations. The blue traces are the DGCPM model run without data assimilation.

- Based on the Weimer (2002) basis function set

$$\Phi(\theta, \phi) = \sum_{l=0}^{4} \sum_{m=0}^{min(l,3)} (A_{lm} \cos m\phi + B_{lm} \sin m\phi) P_l^m(\cos\theta),$$

- Assoc. Legendre Polynomials
- Periodic angular functions

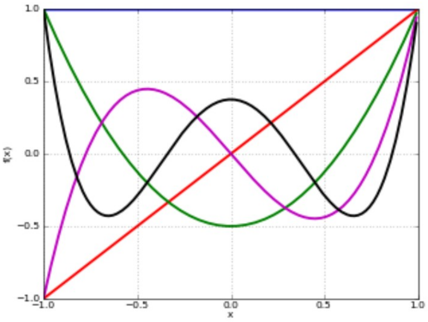

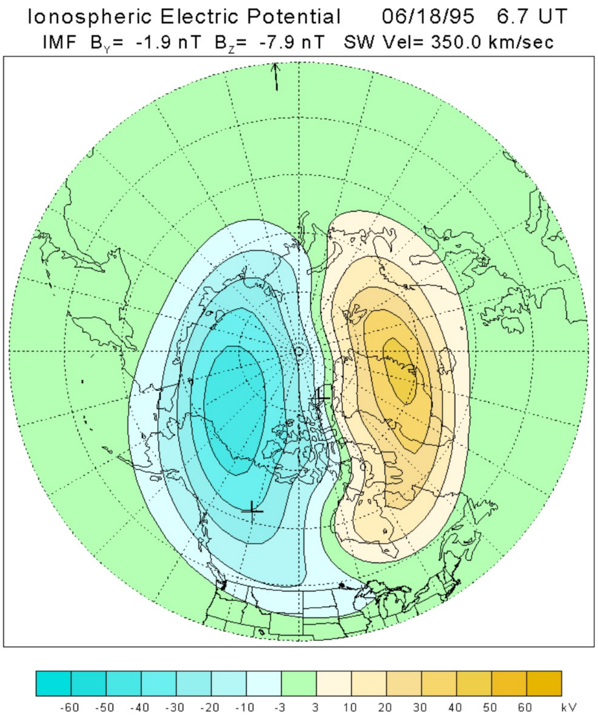

Figure 3.7. Illustration of the harmonic electric potential used for the assimilation.

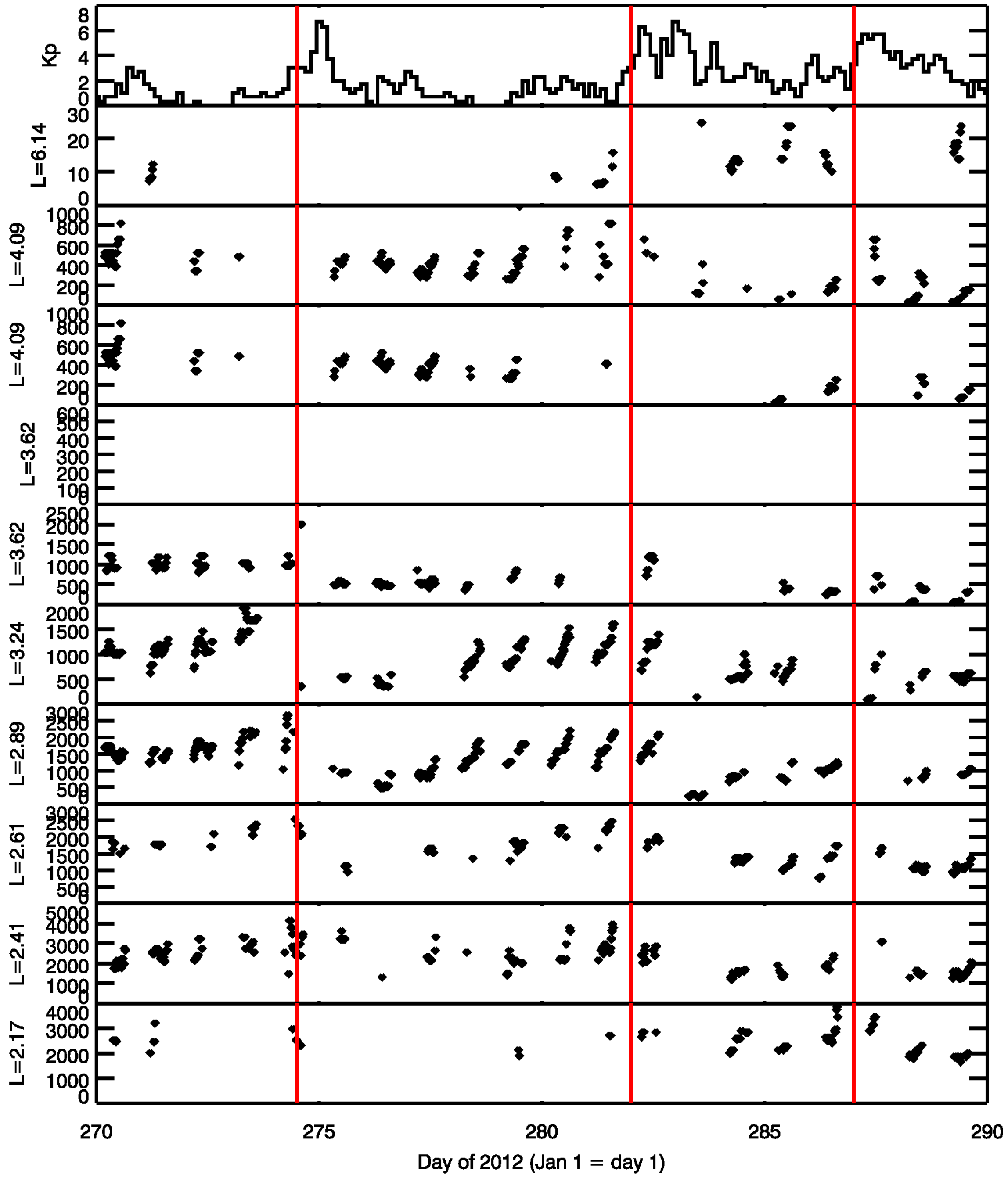

Figure 3.8. Example of a EMMA data set.

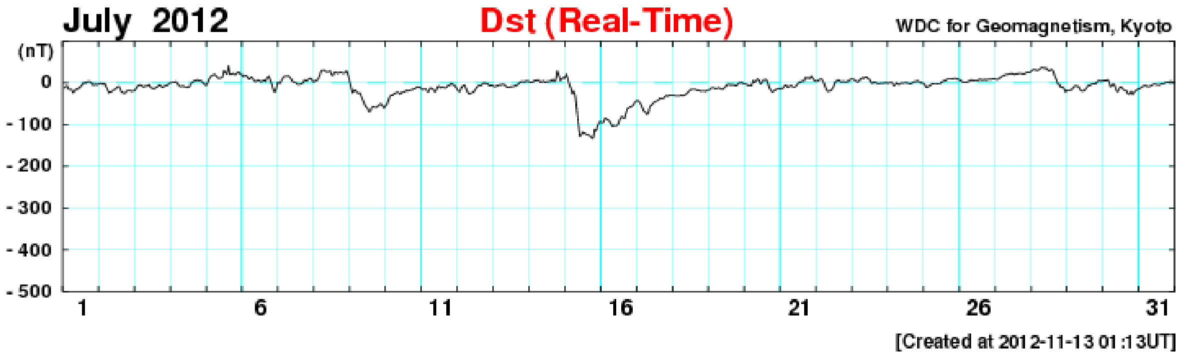

*Figure 3.9.*Dst index for July 2012.

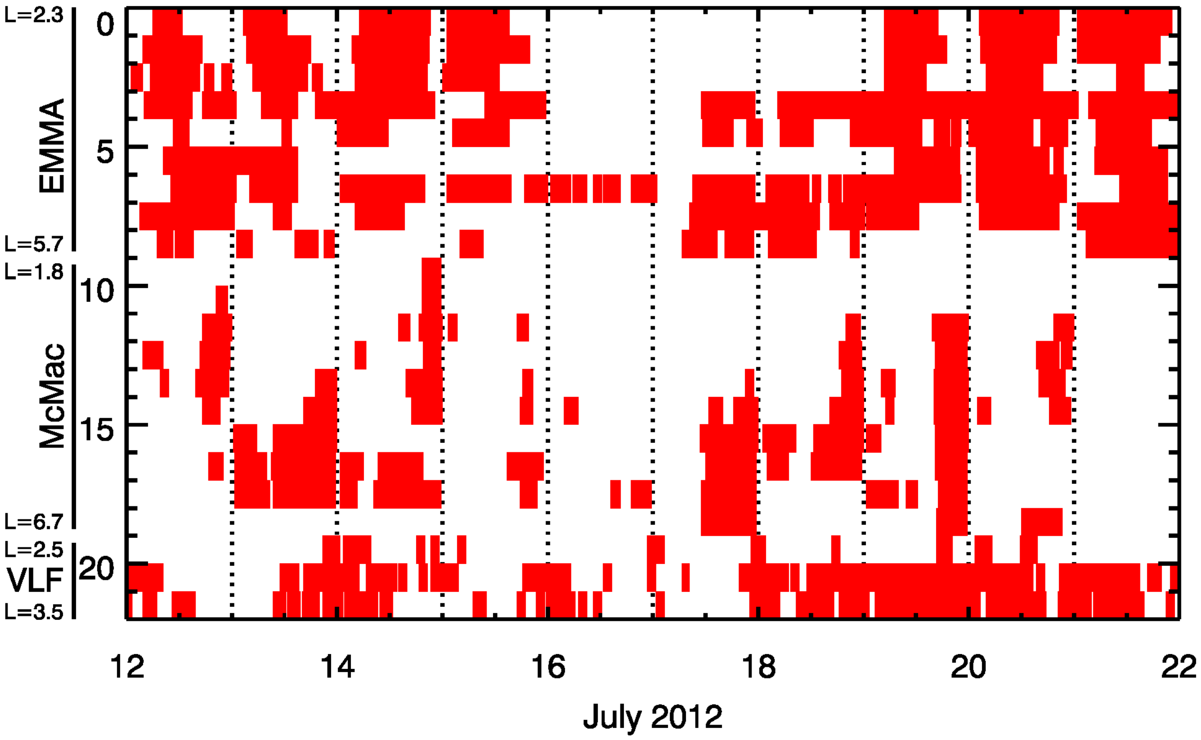

Figure 3.10. Data coverage for the 15 July 2012 storm.

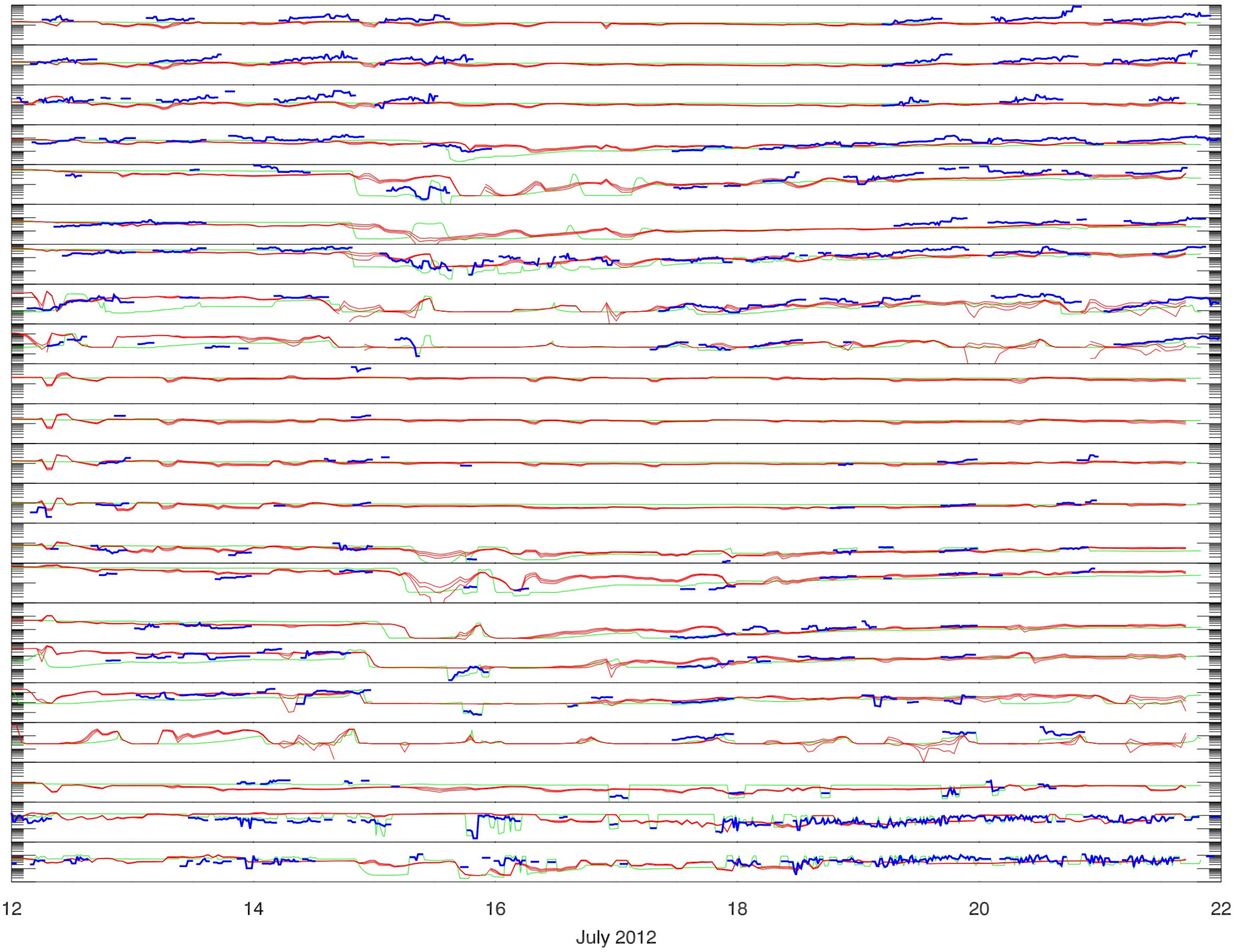

Figure 3.11. Time series of data and assimilation output.

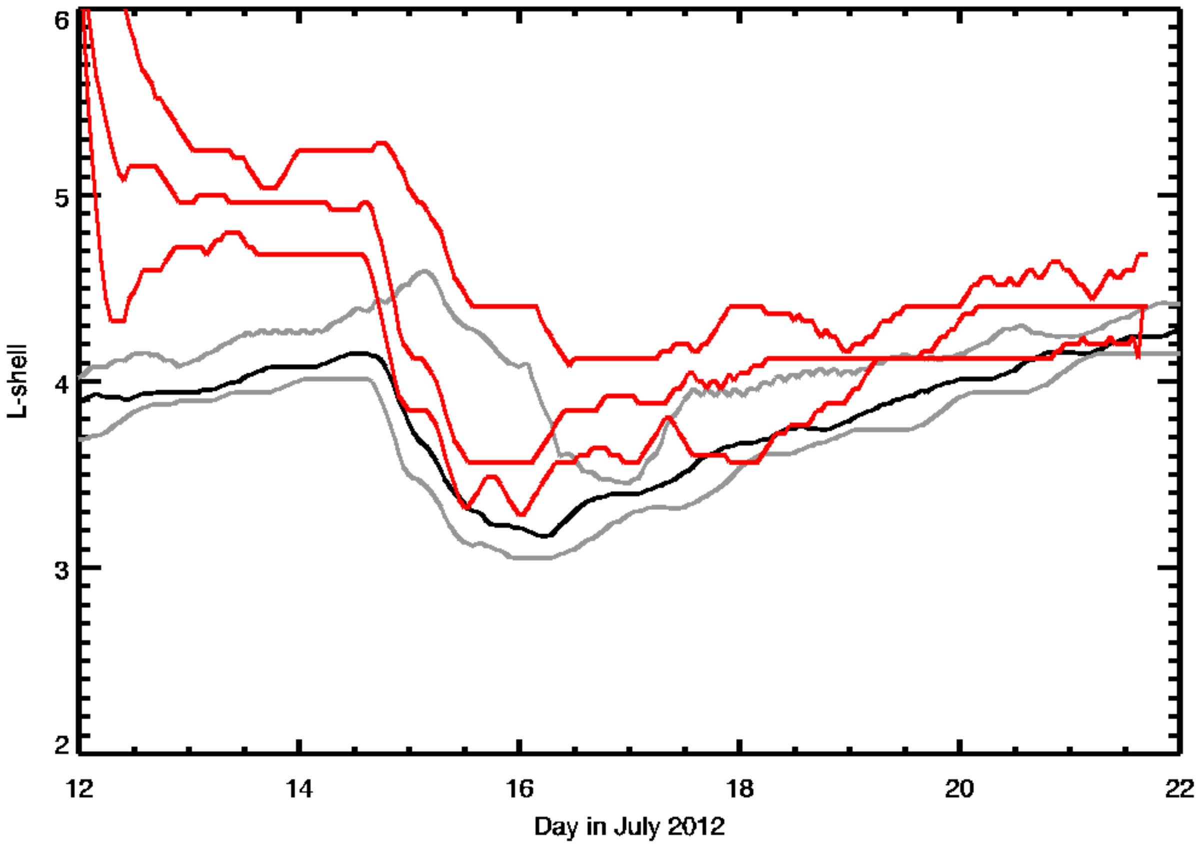

Figure 3.12. The location of the plasmapause derived from the assimilation run, and compared to the plasmapause location from a non-assimilation run. The black and grey lines are the median and range, over MLT, of the location of the plasmapause as a function of time. The red lines are the corresponding, for the assimilation results.

Figure 4.1: The location of the AARDDVARK systems installed as part of PLASMON during year 1 and year 2. The approximate non-disturbed location of the plasmapause is indicated by the dashed line at L=4, and the plot shows that some of the paths from VLF transmitters (green circles) to the new AARDDVARK receivers (red diamonds) are inside the non-disturbed plasmasphere, and span a wide range of longitudes – from Europe to western USA.

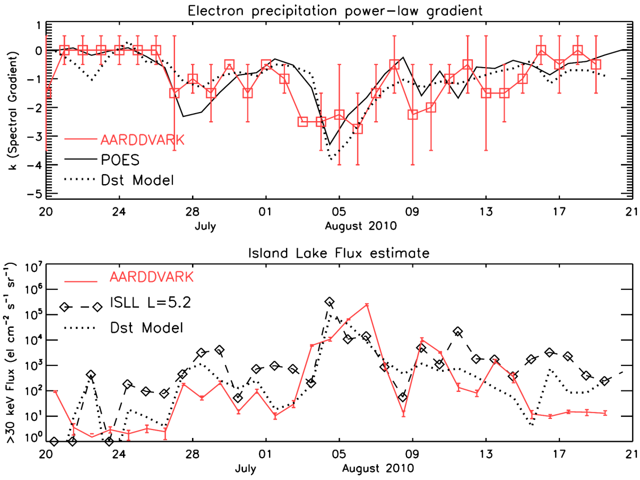

Figure 4.2. Upper panel. The variation in the power-law spectral gradient for POES 3<L<7 BLC fluxes (black) and for the AARDDVARK 3<L<7 perturbations (red). Lower panel. >30 keV electron precipitation flux estimates for the AARDDVARK 3<L<7 data (red line), and the Island Lake riometer absorption data (dashed line with diamonds). In the panels the dotted line represents simple models of the spectral gradient and precipitating flux respectively based on the daily Dst index.

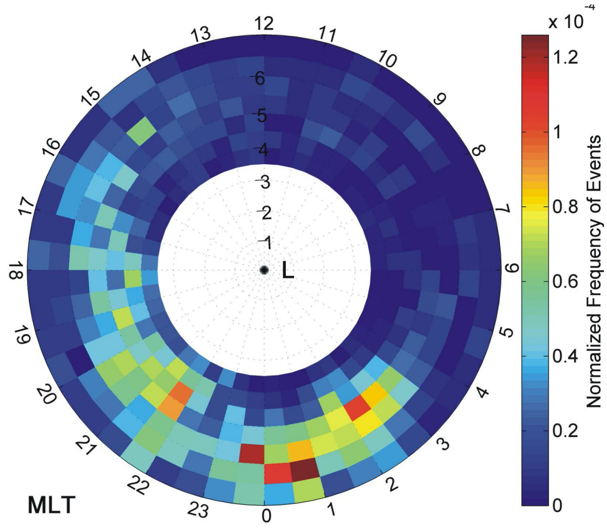

Figure 4.3. The distribution of events detected by IGRF L-value and MLT, where L increases from 0 – 7 *Re* outwards from the centre. The majority of events are located near L~5, and biased towards the evening and night-time sectors.

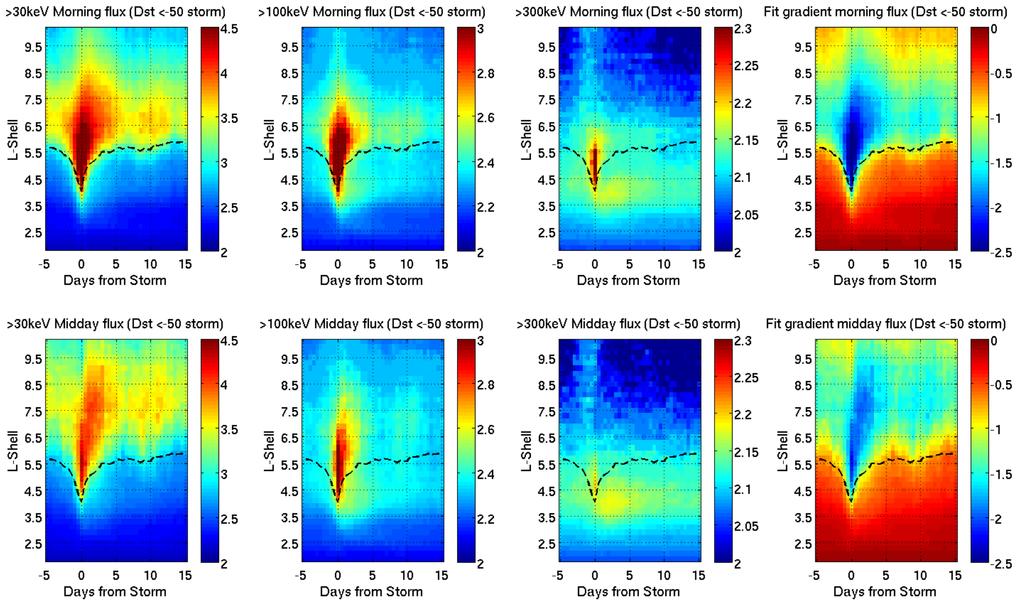

Figure 4.4: POES >30, >100, >300 keV precipitation fluxes induced by chorus relative to the dynamic variation of the plasmapause during a superposed epoch analysis of geomagnetic storms. Upper panels: the morningside chorus-driven precipitation tends to occur primarily outside the plasmapause, and with power-law spectral gradients of -2. Lower panels: the daysideplasmaspheric hiss-driven precipitation tends to occur inside the plasmapause and appears nearly mono-energetic ~300 keV.

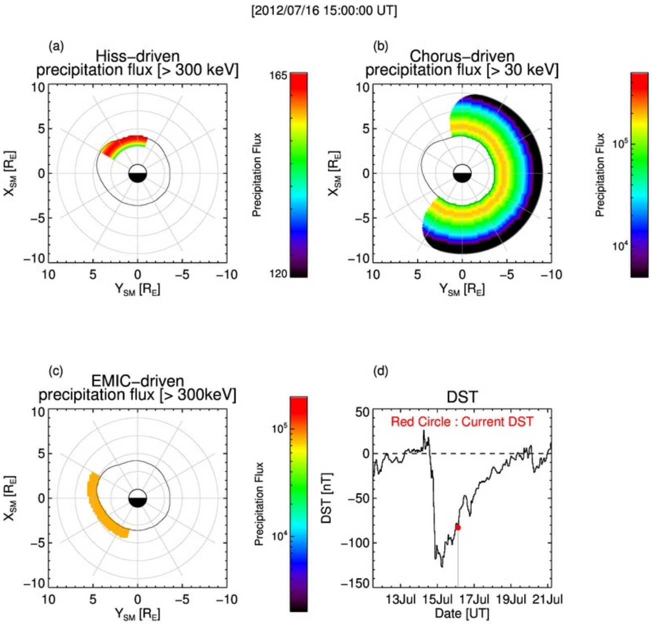

***Figure 4.5**: An example of the WP3-WP4 integrated precipitation model fluxes plotted [flux in e*$^-$*/ (cm*^{2}*.sr.s)] during disturbed geomagnetic conditions, using the PLASMON WP3 plasmapause. The model shows 3 clock panels of MLT versus L-shell, with a plasmapause shown by the circular feature at about L=3. Upper left panel shows plasmaspheric hiss fluxes inside the plasmapause on the dayside (indicated by the light half of the circle which* represents the Earth, and Sun to the top of the panel). Upper right shows the chorus fluxes outside the plasmapause. Lower left panel shows the EMIC-driven fluxes on the plasmapause. Lower right panel shows the variation of

the geomagnetic activity index Dst during the study period.

Equations 4.2:

1. **The algorithms for flux occurring OUTSIDE of the plasmapause, i.e., chorus:**

$$\mathrm{flux}_{\mathrm{chorus}(>30\mathrm{keV})} = C_1\,|\,\mathrm{Dst}\,|^{2.8} + C_2 ,$$

The coefficients are dependent on L-shell:

$$C_1 = 0.6975e^{-\alpha_1^2} + 0.212e^{-\alpha_2^2} , \quad C_2 = 904e^{-\alpha_3^2} + 9.65 \times 10^{16} e^{-\alpha_4^2} ,$$

Additionally, the spectral power-law for the precipitating flux:

$$\mathrm{gradient}_{\mathrm{chorus}} = C_4 . \mathrm{Dst} + C_5$$

With L-shell dependent coeffs of:

$$C_4 = 0.02e^{-\alpha_6{}^2} + 0.027e^{-\alpha_7{}^2} , \quad C_5 = 0.861e^{-\alpha_8^2} + 0.4744e^{-\alpha_9^2} ;.$$

Where the exponents are:

$$\alpha_1 = \frac{s-1.007}{0.962} , \quad \alpha_2 = \frac{s-2.295}{1.43} , \quad \alpha_3 = \frac{s-1.77}{1.27} , \quad \alpha_4 = \frac{s-431}{75} ,$$

$$\alpha_6 = \frac{s-0.438}{1.53} , \quad \alpha_7 = \frac{s-2.82}{2.5} , \quad \alpha_8 = \frac{s-1.05}{1.51} , \quad \alpha_9 = \frac{s-3.245}{1.395} ;$$

featuring the parameter:

$$s = L - L_{pp} .$$

2. **The algorithms for flux occurring INSIDE of the plasmapause, i.e., hiss:**

$$\mathrm{flux}_{\mathrm{hiss}(>300\mathrm{keV})} = C_3\,|\,\mathrm{Dst}_{t-48\mathrm{h}}\,|^{0.065}$$

Where $C_3 = 119e^{-\alpha_5{}^2}$, and $\alpha_5 = \frac{L-4.1}{3}$

3. **The algorithms for flux occurring ON the plasmapause, i.e., EMIC waves:**

$$\mathrm{flux}_{\mathrm{EMIC}(>300\mathrm{keV})} = \begin{Bmatrix} |\,\mathrm{Dst}\,| \times 10^3 : \mathrm{Kp} \geqslant 4 \\ 0 : \mathrm{Kp} < 4 \end{Bmatrix} ,$$

Power-law $\mathrm{gradient}_{\mathrm{EMIC}} = -2.5$.